



Degradation mechanism and QSAR models of antibiotic contaminants in soil by MgFe-LDH engineered biochar activating urea-hydrogen peroxide

Qincheng Chen^a, Zhiwen Cheng^b, Xiaoying Li^a, Chen Wang^a, Lili Yan^c, Guoqing Shen^{a,*}, Zhemin Shen^{b,d,e}

^a School of Agriculture and Biology, Shanghai Jiao Tong University, 800 Dongchuan Road, Shanghai 200240, PR China

^b School of Environmental Science and Engineering, Shanghai Jiao Tong University, 800 Dongchuan Road, Shanghai 200240, PR China

^c School of Chemistry and Chemical Engineering, Shanghai University of Engineering Science, 333 Longteng Road, Shanghai 201620, PR China

^d State Environmental Protection Key Laboratory of Environmental Health Impact Assessment of Emerging Contaminants, Shanghai 200240, PR China

^e Shanghai Engineering Research Center of Solid Waste Treatment and Resource Recovery, Shanghai 200240, PR China

ARTICLE INFO

Keywords:

MgFe-LDH engineered biochar

Urea-hydrogen peroxide

Catalytic degradation

QSAR

Antibiotics

ABSTRACT

Developing an *in-situ* soil remediation technology for simultaneous catalytic degradation of contaminants and nitrogen supplementation is of great importance but remains challenging. Herein, MgFe-LDH engineered biochar (MB) was successfully synthesized by using a simple co-precipitation method. The as-prepared materials were used as catalysts for the first time to activate urea-hydrogen peroxide (UHP) to degrade antibiotic sulfamethoxazole (SMX) and provide nitrogen. The enhanced degradation efficiency of SMX (91%) were mainly attributed to $\bullet\text{OH}$ and $^1\text{O}_2$ -mediated oxidation. Pot experiments showed MB/UHP significantly decreased the SMX concentration from 6.47 to 2.10 mg kg⁻¹ and simultaneously increased NH₄⁺-N and NO₃⁻-N concentration. The optimal quantitative-structure-activity-relationship model for 19 antibiotics suggested the dipole moment, energy of the highest occupied molecular orbital, and bond order were the intrinsic influencing factors. This study not only provides a green remediation technology but also offers a theoretical basis for estimating the removal rate of unexplored antibiotics.

1. Introduction

Antibiotics are extensively produced and used worldwide every year. For example, the annual antibiotic production capacity of China is approximately 210,000 tons [1]. A total of 17,000 tons (15 million kg) of antibiotics are used annually in the United States and 80% in agriculture [2]. Overuse of antibiotics leads to serious global environmental issues [3]. To date, numerous publications have focused on antibiotic degradation during wastewater treatment processes [4–6], but few investigations have been published on antibiotic-contaminated soil remediation [7]. Song et al. explored SMX removal using multi-soil-layering system in rural area [8]. Zhou et al. reported that activation of peroxydisulfate by nanoscale zero-valent iron exhibited excellent effect for SMX removal from agricultural soil [9]. However, few technologies can simultaneously remove soil antibiotic contaminants and improve soil fertility. Therefore, a significant challenge is to develop such dual-acting *in-situ* soil remediation technologies. Moreover, it is difficult to predict the degradation behavior parameters for the

extended list of antibiotics, especially when experimental identification is technically challenging.

Biochar, as an efficient sorbent of contaminants, has great agricultural and environmental potential application [10]. However, antibiotic contaminant-loaded biochar in the environment involves the risk of becoming a secondary source of pollution [11]. In recent years, considerable attention has been paid to the catalytic degradation ability of biochar [12]. Researchers have suggested that hydroxyl radicals ($\bullet\text{OH}$), which can be formed from persistent free radicals on the surface of biochar, play the main role in the degradation of organic contaminants [13]. Among various influencing factors, the choice of oxidant is a remarkable property that enables effective antibiotic degradation, yet few oxidants have been reported to have acted as the source to simultaneously produce $\bullet\text{OH}$ and offer soil fertility. Therefore, selecting an appropriate oxidant is critical to the successful development of *in-situ* soil remediation technology.

Urea-hydrogen peroxide (UHP, CO(NH₂)₂·H₂O₂) has been reported to be an excellent soil conditioner, which is beneficial to improving soil

* Corresponding author.

E-mail address: gqsh@sjtu.edu.cn (G. Shen).

<https://doi.org/10.1016/j.apcatb.2021.120866>

Received 25 June 2021; Received in revised form 24 October 2021; Accepted 26 October 2021

Available online 30 October 2021

0926-3373/© 2021 Elsevier B.V. All rights reserved.

aeration, increasing the utilization rate of nitrogen in the soil, and promoting crop growth [14]. More importantly, UHP is a solid peroxide-based oxidant, which is a stable and easy-to-handle reagent, and can dissociate into urea and H_2O_2 in water [15]. Frabksnberger et al. [16] reported that UHP can be used successfully in remediation of petroleum hydrocarbons and improving soil nitrogen utilization and soil aeration. Our previous study also demonstrated that Fe-impregnated biochar could catalyze UHP to degrade 75.06% 1,3-dichloropropene after 24 h and simultaneously promote lettuce growth [17]. However, the adsorption capacity of Fe-impregnated biochar is poor, which limits its catalytic degradation ability.

Kang et al. [18] reported that layered double hydroxides (LDHs) engineered biochar showed excellent sorption ability because LDHs themselves are robust sorbents due to their layered stacking with type 3R structure and the strong anion exchange capacity. Tan et al. [19] reported that the sorption capacity MgAl-LDH-engineered biochar for tetracycline could reach $1118.12 \text{ mg g}^{-1}$. In addition, some LDHs have shown catalytic degradation ability. For example, Guo et al. [20] demonstrated that CoCu-LDH had good catalytic activity and high stability during the sulfamethoxazole degradation. However, few studies have been conducted on the catalytic degradation ability of LDH-engineered biochar. Therefore, we assume that MgFe-LDH-engineered biochar (MB) is able to catalyze UHP to degrade antibiotics in soil.

Quantitative-structure-activity-relationship (QSAR) models based on density functional theory (DFT) have attracted much attention for predicting degradation behavior in recent years. QSAR models summarize a supposed relationship between chemical/biological properties and the structure of a dataset of molecules through mathematical fitting. The chemical/biological properties can be interpreted by the quantum chemical parameters from the perspective of molecular structures, and thus estimate the properties of unexplored chemicals [21,22]. Previous QSAR studies have shown that the degradation rules of organic contaminants can be attributed to structural quantum chemical parameters (e.g., orbital energy [23], bond order [24], and Fukui indices [25]) during oxidation processes (e.g., ozonation [26], sulfate radical oxidation [27], and hydroxyl radical oxidation [28]). Recently, some studies have applied QSAR models to explore the degradation of antibiotics. For example, Huang et al. [29] established a QSAR model for sulfonamides and revealed that the degradation rule of SAs mainly relates to atomic partial charge on C atoms, HOMO energy, and Fukui index with respect to nucleophilic attacks. Luo et al. [30] developed an optimal QSAR model that contained three structural descriptors (i.e., number of CH_2RX fragments, atomic partial charge on C atoms, and dipole moment) for the dissociation species of fluoroquinolones and sulfonamides. Despite these promising results, few QSAR models have been applied to the catalytic degradation of antibiotics by biochar.

The overall goal of our study is to develop a novel soil remediation technology by synthesizing MB to activate UHP that effectively degrades antibiotic contaminants and also improve soil nitrogen fertility. Specifically, SMX was used as a target pollutant to investigate the application and degradation mechanism of MB-activated UHP. Subsequently, early-stage seedling growth experiments were used to verify the nitrogen supplement of MB/UHP. Furthermore, other 18 antibiotics were selected to verify the catalytic degradation ability of this technology. Additionally, QSAR models are established to explore the intrinsic factors that affect the degradation characteristics and reveal the degradation rules of antibiotics in this system, as well as offer a rapid and accurate approach to evaluate the degradation behavior of unexplored antibiotics.

2. Materials and methods

2.1. Materials

SMX (99.6%) was purchased from AppliChem (Darmstadt,

Germany). UHP (99.6%) was from Tengzhou Guoan Chemical Co. Ltd. (Shandong, China). Methanol (HPLC grade) was from ANPEL Laboratory Technologies Inc. (Shanghai, China). Isopropanol and *p*-benzoquinone (AR, 98%) were obtained from Shanghai Macklin Biochemical Co. Ltd. Ferrous sulfate heptahydrate ($\text{FeSO}_4 \cdot 7\text{H}_2\text{O}$), magnesium chloride hexahydrate ($\text{MgCl}_2 \cdot 6\text{H}_2\text{O}$), sodium hydroxide (NaOH), and other chemicals were of analytical grade and purchased from Shanghai Titan Scientific Co. Ltd.

2.2. Preparation of MBs

The biochar was derived from corn straw, which was milled into approximately 2 mm powder particles prior to use. The corn straw powder was placed in a covered porcelain crucible and then pyrolyzed under oxygen-limited conditions in a temperature-programmable muffle furnace. The temperature of the muffle furnace was increased at a heating rate of $10^\circ\text{C min}^{-1}$, and 600°C was maintained for 2 h. Biochar was milled and sieved through a $<2 \text{ mm}$ filter before use. To investigate the optimal biochar loading amount, a series of MBs with different weights of biochar were prepared. The process is as follows: 100 mL aqueous solution containing MgCl_2 (0.03 mol) and FeCl_3 (0.01 mol) was first prepared. Then, 0.25, 1, 2.5, 5, and 10 g biochar were added and stirred for 30 min, respectively. The corresponding final products were denoted as MBx ($x = 0.25, 1, 2.5, 5, \text{ and } 10$). Finally, the pH of 100 mL for this mixed solution was adjusted to 10 with 1 mol/L NaOH aqueous solution. The obtained slurry was aged for 72 h at 80°C , followed by centrifugal process, and then thoroughly washed with deionized water. After washing, MBx was obtained by drying at 50°C in an oven.

2.3. Characterizations

Scanning electron microscope (SEM) imaging analysis was conducted by using a Hitachi S4800 SEM. Energy dispersive X-ray spectroscopy (EDX, Horiba 7593-H) was used to monitor surface element. X-ray diffraction (XRD) patterns were recorded on a Bruker D8 Advance X-ray diffractometer with Cu K α irradiation source and operated at 40 kV and 30 mA. Data were collected within a 2θ range of $0\text{--}80^\circ$ at a scan rate of $10^\circ/\text{min}$. The hydrodynamic size and surface charge (zeta potential) of MBs were characterized with a Zeta potential and nanoparticle characterization (Brookhaven Instruments Corp., USA). The ICP-OES (PerkinElmer, Optima 8000) was used to determine the Mg and Fe metal concentration of MBs after being digested by concentrated nitric acid. X-ray photoelectron spectroscopy (XPS) spectra for the original MBs before SMX sorption, after SMX sorption and degradation by an AXIS Ultra DLD with a monochromatic Al K α X-ray source (1486.6 eV), and analyzed with Casa XPS software (version 2.3.12.8). Total organic carbon (TOC, mg C L^{-1}) was determined using the TOC analyzer Multi N/C 3000 (ChD). EPR measurement was conducted on a Bruker ELEXSYS 580 spectrometer to detect $^1\text{O}_2$ using 2,2,6,6-tetramethylpiperidine (TEMP) as spin-trapping agent. The particle sizes were measured using a Horiba LA 930 (Horiba Instruments Inc., Irvine, CA) laser scattering particle size and distribution analyzer. Transmission electron microscopy (TEM, FEI Talos F200x) was performed to further characterize morphology and structure. The average thickness of the layer was measured by the Nano Measurer software.

2.4. Adsorption experiments

Batch adsorption experiments of SMX on MgFe-LDH, biochar and MBx samples were examined by mixing 0.25 g of the adsorbent with 25 mL 10 mg L^{-1} SMX solution in the dark and glass flasks. The flasks were shaken at 200 rpm in an orbital shaking incubator for 24 h at room temperature. At appropriate time intervals (0, 2, 4, 12, and 24 h), the mixtures were passed through a $0.22 \mu\text{m}$ membrane to determine the SMX concentration in filtrates. Adsorption behaviors of SMX on MBs were investigated in terms of kinetic modeling studies. Adsorption

kinetics used pseudo-first-order, pseudo-second-order, and Elovich equations for the regression analysis. The expressions are as follows:

Pseudo-first-order equation:

$$q_t = q_e (1 - e^{-k_1 t}) \quad (1)$$

Pseudo-second-order equation:

$$q_t = \frac{k_2 q_e^2 t}{(1 + k_2 q_e t)} \quad (2)$$

Elovich equation:

$$q_t = \frac{1}{\beta} \ln \alpha \beta + \frac{1}{\beta} \ln t \quad (3)$$

where q_t is the adsorption amount of SMX by MBs at time t , mg g^{-1} ; q_e is the adsorption amount of SMX by MBs at equilibrium, mg g^{-1} ; k_1 is the pseudo-first-order equation adsorption rate constant, h^{-1} ; t is the adsorption time, h ; k_2 is the pseudo-second-order equation adsorption rate constant, $\text{g mg}^{-1} \text{h}^{-1}$; α is the initial adsorption rate ($\text{mg g}^{-1} \text{h}^{-1}$); and β is desorption rate (g mg^{-1}) constant.

Reverse-phase high-performance liquid chromatography equipped with a 5 μm Supelcosil LC-18 column at 25 °C and a Shimadzu LC-20AT pump was conducted to determine SMX concentration in the leachate samples. A Sama UV-Vis LC-830 detector at 274.0 nm was used to detect SMX. Methanol/0.01 mol/L acetic acid solution (70/30 v/v) as flow phase was at 1.0 mL min^{-1} .

2.5. Catalytic degradation activity in aqueous solution

Seven treatments were conducted with three replicates, namely, biochar, biochar/UHP, MgFe-LDH/UHP, MB0.25/UHP, MB1/UHP, MB2.5/UHP, MB5/UHP, MB10/UHP, and UHP in the degradation experiments. MgFe-LDH or MBx (25 mg) was added to 10 mg L^{-1} of SMX aqueous solution (25 mL). After the adsorption equilibrium, the catalytic degradation of SMX was initiated by adding UHP (400 mg). The experiments were conducted in the dark. The SMX concentration of filtrates filtered through a 0.22 μm membrane was determined by the methods described.

2.6. SMX degradation in soil and early seedling growth

Four treatments were conducted with three replicates in SMX degradation and pot experiment; these treatments were as follows: CK (8 mg kg^{-1} of SMX), MB (100 g of treated soil with 8 mg kg^{-1} SMX amended with 0.5% MgFe LDH biochar), UHP (100 g of treated soil with 8 mg kg^{-1} SMX amended with 1% UHP), and MB/UHP (100 g of treated soil with 8 mg kg^{-1} SMX amended with 0.5% MgFe LDH biochar and then with 1% UHP). Determination of SMX concentration in soil was based on the previous method. Briefly, soil samples (1.5 g) were extracted with buffer solution (15 mL) consisting of methanol (7.5 mL), Na_2EDTA (2.5 mL, 0.1 M), and citrated buffer (5 mL, $\text{pH} = 4$). The mixture was shaken at 200 r min^{-1} for 1 h, sonicated for 15 min, and centrifuged at 4000 r min^{-1} for 5 min, and then the supernatant was collected. This extraction procedure repeated three times. The efficiency of SMX recovery through this procedure was approximately 80%. The SMX concentration was determined by the aforementioned methods. After the SMX degradation in soil, three lettuce seeds were sown evenly in each pot to a depth of 2 cm. The optimal plant in each plot after germination was selected for further cultivation. After 60 d of cultivation, nitrogen concentration in soil was measured. Ammonium and nitrate in soil were extracted by 1 M KCl (1:5 w/v), and then determined using a SmartChem 2000 automatic discrete analyzer (Alliance Instruments, France). The weight of lettuce in each pot was also determined.

2.7. Establishment methodology for QSAR model

A total of 18 quantum chemical parameters were included to better expound the molecular properties, and were calculated by Gaussian 09 [31] and Materials Studio 7.0 DMol3 [32] programs based on density functional theory (DFT). Detailed information on the quantum chemical calculation and QSAR model construction method were addressed in Texts S1 and S2 of the Supplementary Material. Briefly, in Gaussian function, the calculation method and basis set were B3LYP and 6-311G+ (d, p), respectively. Additionally, the solvation effect was considered with an implicit water model to better describe the molecular situation in real solution. In Materials Studio 7.0, B3LYP method in DMol3 module was selected to match the results of Gaussian 09. Subsequently, QSAR models were developed using a stepwise multiple linear regression (i.e., MLR) method with removal efficiencies (i.e., Re %) as dependent variables and 18 quantum chemical parameters as independent variables. Finally, the optimal QSAR model was validated based on a series of criteria (Text S2).

2.8. Statistical analysis

Statistical analysis was conducted using OriginPro 8.5 software. Error bars represented standard errors ($n = 3$). Mean separation was performed based on Tukey's multiple range test. The letters above the error bars indicated that the differences between the results were significant at $p < 0.05$.

3. Results and discussion

3.1. Characterization

Fig. 1(a) shows a schematic of the MgFe-LDH structure, which exhibits the R3m rhombohedral symmetry and typical hydroxalite compound structures. Mg^{2+} or Fe^{3+} cation occupies the center of the octahedron, and the metal octahedrons share the edges to form a 2D sheet. These 2D layers are held by hydrogen bonding between the sheets to build a 3D structure. Fig. 1(b) show the SEM image of MgFe-LDH crystal. The sheet-like LDH of MgFe-LDH in Fig. 1(b) is similar to published patterns [18]. As shown in Fig. 1(c), the TEM image further demonstrates that MgFe-LDH has a flaky structure, while the thickness of the layer is 17.06 nm. The surface of MB1 and MB10 formed layered crystals in Fig. 1(d) and (e). The EDX results in Fig. 1(f) suggest that the main components of the layered crystals are Mg and Fe.

To investigate the chemical composition of the layered crystals, XRD technique was performed. As shown in Fig. 2, unlike original biochar (Fig. S1), the XRD patterns of MBs show sharp and symmetric reflections for (003), (006), and (110) planes and wide asymmetric reflections for (009) planes, which is the typical hydroxalite compound structure [33]. The aforementioned SEM and XRD results suggest that MgFe-LDH compounds were successfully synthesized and grafted on biochars in our study. The morphology of the MB samples in Fig. S2 shows that as the ratio of adding biochar increases, the red becomes lighter, the black is darker.

To further explore the effect of biochar on chemical composition in MBs, ICP-OES is conducted to test Mg and Fe contents and results are shown in Table S1. The molar ratios of Mg/Fe in MgFe-LDH is 3.13, similar to that of their precursor, 3.00. More importantly, the increase of biochar weight in MBs causes the increase first and then decrease of the Mg/Fe molar ratio. MB1 has the lowest Mg/Fe molar ratio of 0.783. This condition reflects that adding biochar under hydrothermal conditions influences the chemical composition of LDH, which may be attributed to the reduction effect of biochar. When the weight of biochar is up to 2.5 g, the diffraction peak at 26.51° appears, which corresponds to akaganeite ($\text{FeO}(\text{OH})$) curves 5, 6, and 7 in Fig. 2 [34]. As the biochar weight ratio increases, the peak intensity of akaganeite is enhanced. According to the XRD patterns, the lattice parameters are calculated and

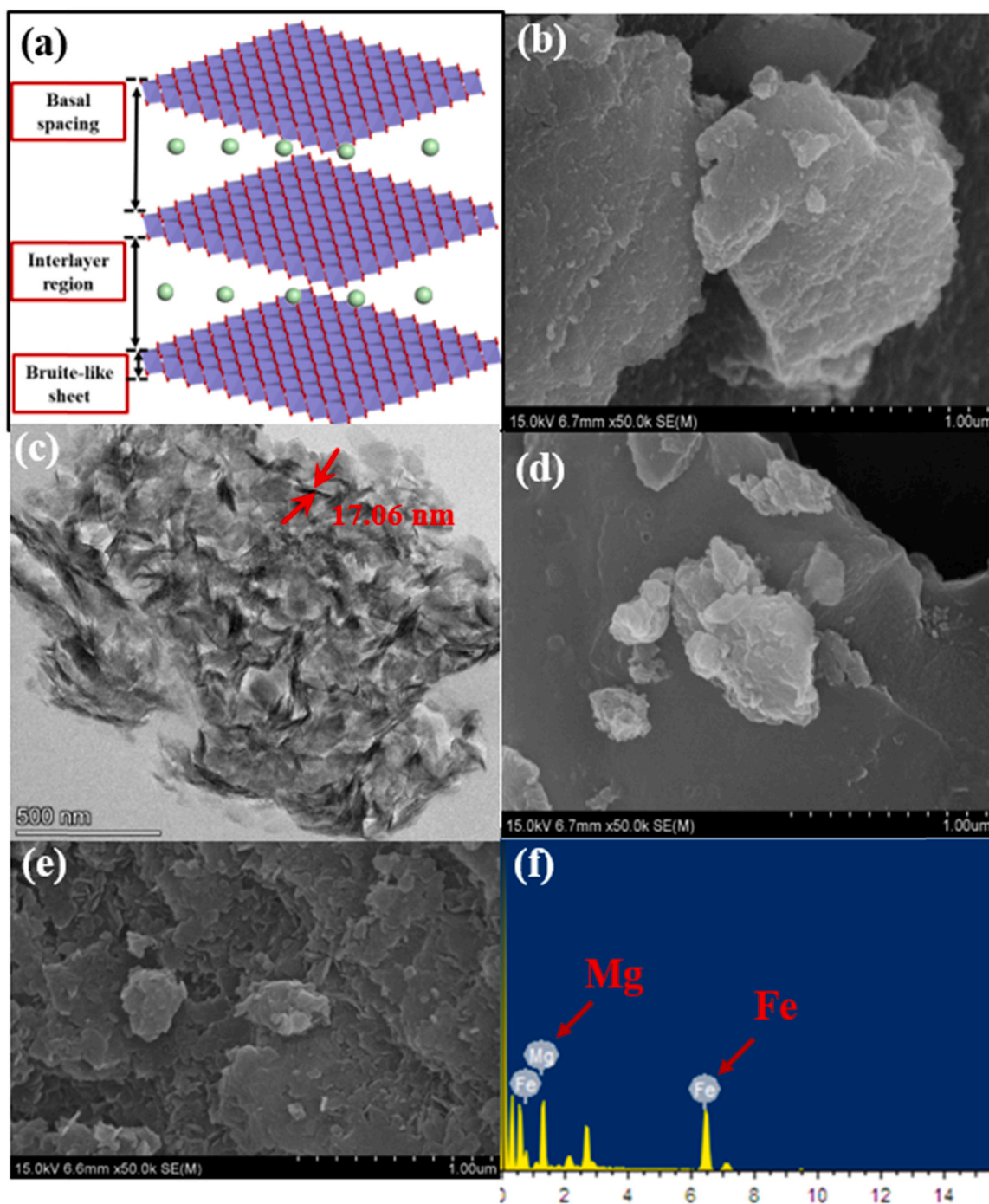


Fig. 1. Schematic illustration of MgFe-LDH (a), SEM image (b) and TEM image (c) of MgFe-LDH, SEM images of MB1 (d) and MB10 (e), and EDX patterns of MB1 (f).

shown in Text S3 and Table S1. As shown in the table, peak intensity and sharpness of MgFe-LDH, as a measure of crystallinity, decreases from 3907 Cps (MgFe-LDH crystals) to 1468 Cps (MB10) with the increase of biochar weight (Table S1). These changes are due to the low crystallinity of MgFe-LDH as biochar weight increases. Note that MgFe-LDH is still the dominant crystal in the view of the weaker peak intensity of akaganeite compared with that of MgFe-LDH.

3.2. Adsorption ability by MBs

The removal ability of the MBs/UHP toward antibiotics was initially evaluated by using SMX as a model pollutant. The first and key step in the degradation process is the adsorption of target pollutants on the

degradation material to prepare for the attack of radicals [35]. In this study, biochar showed negligible SMX sorption capacity (Fig. S3). Therefore, the sorption of MB was dominated by MgFe-LDH rather than biochar matrix. For a complete understanding of the adsorption properties of MBs/UHP, adsorption kinetic studies of MBs were conducted and the results are presented in Fig. 3. The adsorption process rapidly occurred in the initial 2 h and then nearly reached equilibrium after 4 h. The adsorption data showed a better fit with the pseudo-second-order kinetic model ($R^2 > 0.99$) than the pseudo-first-order and Elovich models (Table S2), suggesting that the adsorption process was chemisorption rather than physisorption. More importantly, with the increase of biochar weight, the adsorption capacity of MBs first increases and then decreases. The MB1 showed the highest q_e value of 2.271 mg g^{-1} ,

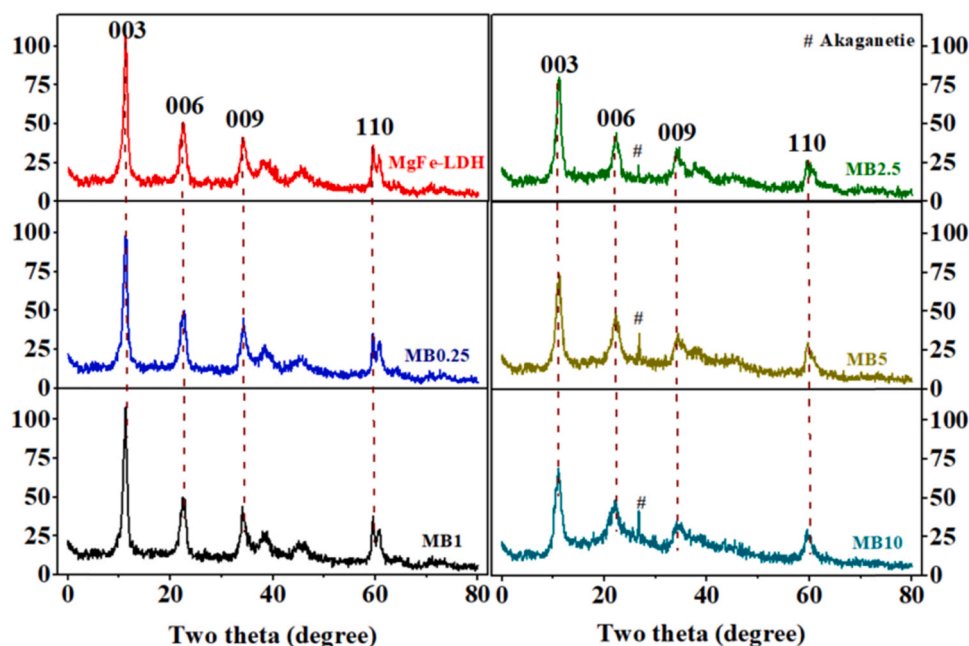


Fig. 2. XRD patterns of MgFe-LDH, MB0.25, MB1, MB2.5, MB5 and MB10.

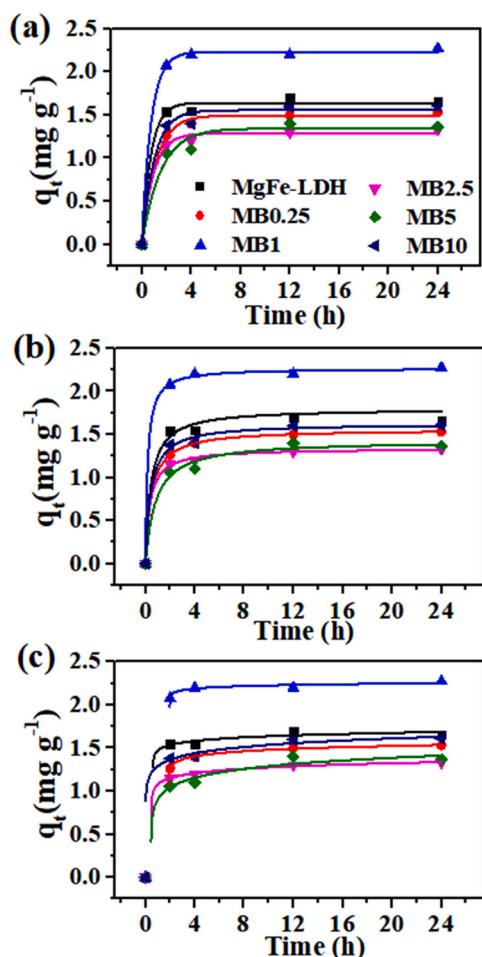


Fig. 3. Pseudo-first-order (a), pseudo-second-order (b), and Elovich (c) adsorption kinetic modeling results of SMX on MgFe-LDH and MBs samples. (Experimental conditions: [MBs] = 25 mg L⁻¹, [SMX] = 10 mg L⁻¹ for kinetic studies).

according to the pseudo-second-order kinetic modeling analysis. A reasonable explanation for this result is that the addition of biochar with proper weight ratio reduces the agglomeration of MgFe-LDH and then increases the adsorption capacity of MBs.

To test the agglomeration of MgFe-LDH, the particle sizes of different samples were obtained and shown in Fig. S4. As the weight of biochar increases, the mean particle size of MB first decreases and then increases. The mean particle size of pure MgFe-LDH crystal is approximately 1780 nm (Fig. S4(a)). The mean particle size of MB1 is 886.95 nm (Fig. S4(b)), which is significantly lower than that of MgFe-LDH crystal. Therefore, adding an appropriate weight ratio of biochar reduces the accumulation of MgFe-LDH and then may promote degradation performance. As the biochar particle is relatively large (2435.74 nm) in Fig. S4(d), when the weight ratio of the biochar continues to increase, the particles of the composition become larger, and the mean particle size of the MB10 is 1337.65 nm (Fig. S4(c)).

Note that SMX adsorption by MB reaches the adsorption equilibrium in a short time, which is different from the usual adsorption performance of original biochar. In addition, previous studies reported that LDH particles with 3D layer-stacked structure can achieve rapid adsorption of pollutants. Therefore, in this study, the sorption of MB may be dominated by MgFe-LDH crystals rather than biochar. Fig. S5 shows that the surface of MgFe-LDH was positively charged, and conversely, biochar was negatively charged (−35.25). The correlation analysis shows a positive correlation between zeta potential and sorption ability of MBs (0.942, $p < 0.01$). These results suggest that the sorption mechanism of SMX by MBs might be related to electrostatic interaction. In addition, the XPS spectra of Mg 2p and Fe 2p of MBs before and after sorption in Fig. S6 showed insignificant change, indicating that the sorption process has no effect on chemical compositions and valence states of Mg and Fe, which further demonstrates that the sorption mechanism might be electrostatic interaction between MgFe-LDH crystals on the surface of MBs and SMX.

3.3. Catalytic degradation performance and mechanism of MB/UHP

After the sorption reaction, approximately 95% adsorbed SMX was extracted, demonstrating that the degradation ability of the MBs alone was negligible. The adsorption reached a complete equilibrium after 24 h, and the catalytic degradation of SMX was initiated by adding UHP.

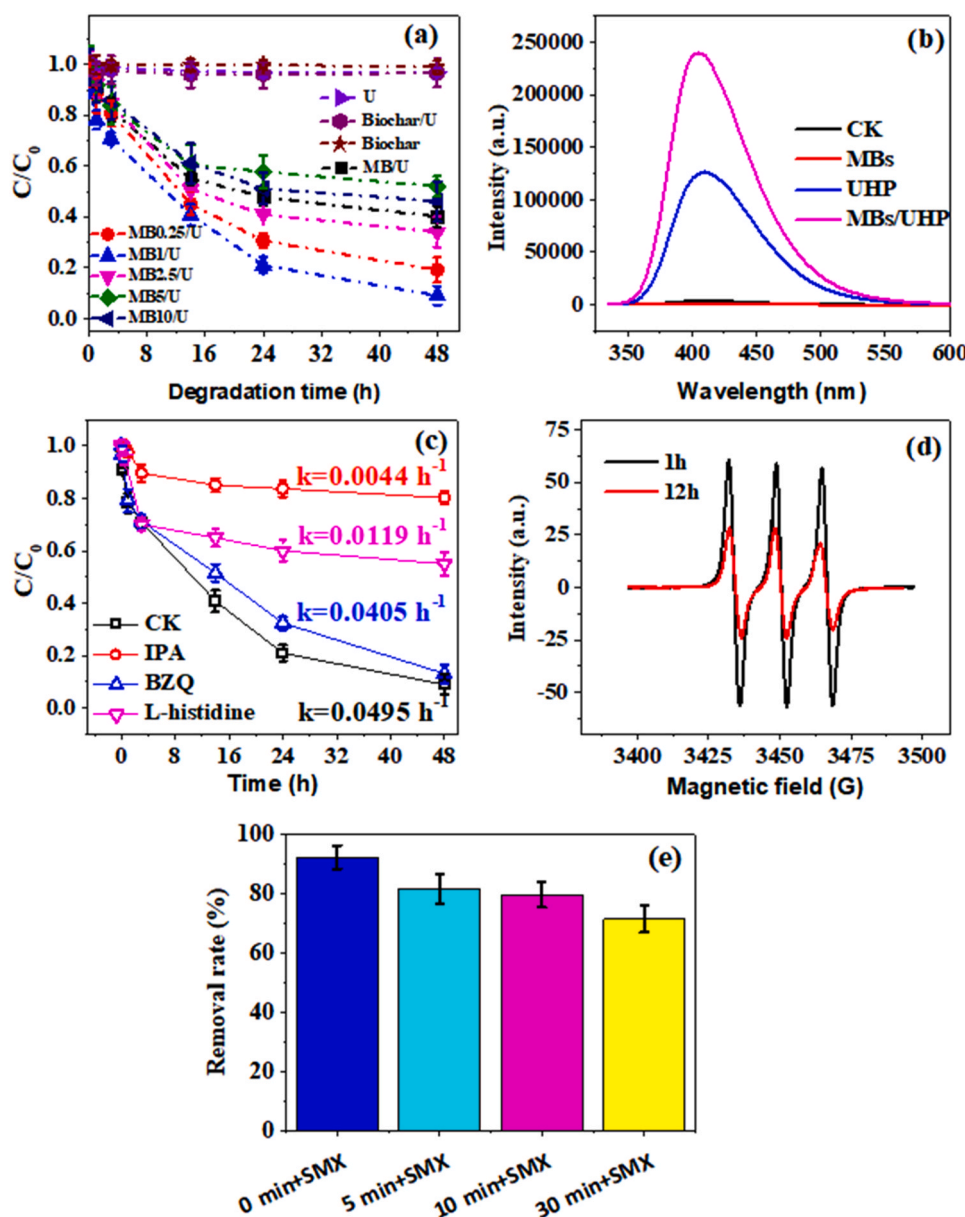


Fig. 4. (a) SMX degradation activities by MBs/UHP; (b) The fluorescence intensity of the emission peak of MB1/UHP; (c) Quenching experiments in MB1/UHP system under different scavengers; (d) EPR spectrum of species adducts trapped by TEMP in MB1/UHP system; (e) The removal efficiency of SMX under different regular time intervals for SMX adding after MB1 and UHP mixing.

Fig. 4(a) shows the SMX degradation performance of MBs/UHP. As can be seen in Fig. 4(a), the treatments of biochar and UHP have negligible degradation for SMX. The SMX degradation rate of MBs/UHP reached 91.0%, whereas the SMX degradation rates of MBs and UHP alone treatment was 3.3% and 3.0%, respectively. These results suggest MgFe-LDH play key role in the degradation process. In addition, the effect of the biochar weight ratio on the SMX degradation ability showed that with the increase of biochar weight ratio, the degradation ability of MBs/UHP first increased and then decreased. The MB1/UHP exhibits the strongest degradation ability, with 91% degradation efficiency of SMX after 48 h. MB1 has higher adsorption capacity and better addition ratio of biochar than other MBs, which reduce the aggregation of MgFe-LDH and improve degradation performance. Pseudo-first-order, pseudo-second-order, and Elovich kinetic models have been used in modeling the kinetics of SMX degradation to elucidate the kinetics of SMX degradation by the MBs/UHP system. Table S3 shows the kinetic parameters for the degradation of SMX by MB1/UHP. The pseudo-second-

order reaction ($R^2 = 0.9133$) describes the SMX degradation better rather than the pseudo-first-order ($R^2 = 0.8340$) and Elovich kinetic ($R^2 = 0.7242$). The degradation rate (k_2) of MB1 based on the pseudo-second-reaction kinetic model is $0.0046 \text{ L mg}^{-1} \text{ h}^{-1}$. This result suggests that the degradation of SMX in the system of MBs/UHP is classified as the second-order reaction kinetic.

The SMX degradation performance demonstrated that MBs/UHP is an excellent catalytic system. MB1/UHP, which exhibited the strongest degradation ability, was selected for further degradation mechanism study. The XRD patterns of the MB1 before and after the degradation showed no significant difference (Fig. S7), indicating the high stability of the LDH. TOC removal rate was used to evaluate the degradation efficiency of organic contaminants [36], and therefore, was determined for MBs/UHP. Fig. S8 illustrates the time course of the TOC variance of the SMX degradation, where the TOC removal rate can reach 53.5% after 72 h, which means that mineralization was achieved. Fig. S9(a) and (b) show the total ion chromatogram of SMX with and without

MB/UHP, respectively. Four new peaks (m/z 274.26374, m/z 97.96451, m/z 218.20319, and m/z 246.23342) were detected in Fig. S9(c). Possible degradation pathways for SMX oxidation in MB/UHP systems were proposed based on the identification of these products (Fig. S10). As shown in Fig. S10, degradation occurred during the cleavage of the sulfonamide bond (m/z 97.96451 and 218.20319) and the formation of the mono-hydroxylated derivative (m/z 274.26374). Additionally, the opening of the isoxazole ring was assessed by the identifying of P4 (m/z 246.23342). These results demonstrate that SMX was degraded, which aligns with the results of previous studies [37–39].

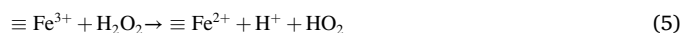
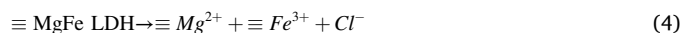
Fig. 4(b) shows the fluorescence intensity of the emission peaks of CK, MB1, UHP, and MB1/UHP solutions at 410 nm 2 h after the solution was prepared. The characteristic fluorescence peak at 410 nm corresponds to $\bullet\text{OH}$ in a terephthalic acid solution [40]. Fig. 4(b) demonstrates that MB1/UHP produced more $\bullet\text{OH}$ than UHP and MB alone, which suggested that $\bullet\text{OH}$ might be one of the reactive oxygen species (ROS) in the MB/UHP system. Ye et al. [41] reported that, in addition to radical pathways containing $\bullet\text{OH}$ oxidation, non-radical pathways containing singlet oxygen ($^1\text{O}_2$) mediated oxidation was elucidated as the predominant pathways in the catalytic degradation of organic contaminants by biochar systems.

To further explore the ROS in the system of MBs/UHP, isopropanol (IPA, 20 mM), *p*-benzoquinone (BZQ, 1 mM), and L-histidine (10 mM) were employed as scavengers for $\bullet\text{OH}$, superoxide anion radicals ($\bullet\text{O}_2^-$) and $^1\text{O}_2$ [42]. In the quenching experiments, $\ln(C_0/C) = kt$ (C_0 : initial SMX concentration and C_t : SMX concentration at contact time t) fit the SMX degradation well (Table S4). Fig. 4(c) shows that adding BZQ to the solution decreased the SMX removal rate from 0.0495 h^{-1} to 0.0405 h^{-1} , indicating that $\bullet\text{O}_2^-$ plays a role in the SMX degradation in the MB1/UHP system. The evident decreases of the SMX removal percentage can be found in the presence of IPA, with the k declining from 0.0495 h^{-1} to 0.0044 h^{-1} , suggesting that $\bullet\text{OH}$ is the predominant active species in this system. Therefore, these results illustrated that $\bullet\text{O}_2^-$ and $\bullet\text{OH}$ were generated and participated in the reaction for the SMX degradation in the MB/UHP system. However, the removal of SMX proceeded even when IPA was in excess for the SMX removal. $^1\text{O}_2$, as a potential reactive oxygen species in a non-radical pathway, was confirmed by quenching experiments with L-histidine. Fig. 4(c) showed that L-histidine led to inhibition of SMX degradation as the calculated reaction k decreased to 0.0119 h^{-1} . This quenching experiment preliminarily proved the existence of $^1\text{O}_2$. The electron spin resonance spectrometer (MS 5000, Magent Tech, Germany) was used to further probe the generation processes of $^1\text{O}_2$ in the MB1/UHP system, in which TEMP was treated as the spin trap. Fig. 4(d) showed an obvious typical three peak signal ($a_N = 17.0 \text{ G}$) of TEMP, showing strong intensity after 1 h and even 12 h, indicating that $^1\text{O}_2$ might be the main reactive species for catalytic degradation in the MB/UHP system.

The distinction between radical-mediated oxidation and non-radical pathway-mediated oxidation can be distinguished by late addition of contaminants after mixing the catalyst and oxidant [41]. If radicals dominated the oxidation process, then a longer delay in adding contaminants would lead to a significant reduction in degradation efficiency due to the short lifetime and constant consumption of the radicals. Fig. 4(e) showed that the SMX removal rate decreased with the increasing time interval for delayed addition of contaminants. However, the removal rate was still 71.54% with the addition of contaminants 30 min later, indicating that the rather high contribution of SMX degradation came from the non-radical pathway of $^1\text{O}_2$.

To further explore the activation mechanism of UHP on MBs, we conducted XPS to determine the chemical states. MgFe-LDH on the surface of the MBs participates in the following chemical reaction in the form of Mg^{2+} and Fe^{3+} (Eq. (4)) [43]. According to the XPS spectra in Fig. S11, before degradation, two peaks are visible at 711.70 eV and 725.30 eV, assigned to $\text{Fe } 2p_{3/2}$ and $\text{Fe } 2p_{1/2}$ of Fe_3O_4 , indicating that MB is composed of Fe^{2+} and Fe^{3+} . After degradation, another two peaks appeared at 713.87 eV and 727.77 eV, assigned to $\text{Fe}^{2+} 2p_{3/2}$ and Fe^{2+}

$2p_{1/2}$. As the ratio of Fe^{2+} : Fe^{3+} in the stoichiometric Fe_3O_4 should be 1:2, the ratio of Fe^{2+} : Fe^{3+} changed before and after degradation. The XPS results prove the existence of transformation from Fe^{3+} to Fe^{2+} during the catalytic process. It is generally accepted that Fe^{2+} reacts with H_2O_2 leading to the generation of $\bullet\text{OH}$ (Eq. (6)), whereas the regeneration of Fe^{2+} by the reaction of Fe^{3+} with H_2O_2 , extending the Fenton process (Eq. (5)) [44]. In addition, H_2O_2 generated an intermediate $\bullet\text{O}_2^-$, $\bullet\text{O}_2^-$ further combined with H_2O molecules to generate $^1\text{O}_2$ (Eq. (7)) [45]. The production mechanism and process of main reactive species are proposed as listed in Eqs. (4–7).



\equiv represents the surface of MBs.

3.4. SMX degradation in soil and bioassay of early seedling growth

Fe impregnated biochar is beneficial to the richness and species diversity of microbial communities in soil [46]. Moreover, UHP has a positive effect on soil aeration and plant growth [47]. Therefore, MB/UHP may be an efficient soil remediation technology that not only repairs soil organic pollution but also improves soil physical and chemical properties to promote crop growth. Fig. 5(a) shows the soil SMX concentration after various treatments. The addition of MB/UHP decreased the SMX concentration from 6.47 mg kg^{-1} to 2.10 mg kg^{-1} , and the results were statistically significant ($p < 0.05$). The results indicated that MB significantly enhanced the degradation efficiency of UHP in soil. $\text{NH}_4^+\text{-N}$ and $\text{NO}_3^-\text{-N}$ are usually the main forms of available nitrogen for plants [48], which are often used to measure the level of soil nitrogen nutrition. As presented in Fig. 5(b), the $\text{NH}_4^+\text{-N}$ concentration of MB/UHP and UHP treatments are 20.82 mg kg^{-1} and 19.67 mg kg^{-1} , significantly higher than that of CK and MB (19.29 mg kg^{-1} and 18.32 mg kg^{-1} , respectively). Similarly, as shown in Fig. 5(c), the concentration of $\text{NO}_3^-\text{-N}$ of MB/UHP and UHP treatments are 10.01 mg kg^{-1} and 9.03 mg kg^{-1} , higher than that of CK and MB (6.29 mg kg^{-1} and 6.04 mg kg^{-1}). Bioassay of early seedling growth, as a simple and commonly used ecotoxicological test, is used to evaluate the effect of biochar amendment on crop growth [49]. After a 49-day growth, the dry weight of lettuce in the UHP and MB/UHP treatments is 75.83 mg , which is significantly higher than that of CK, MB, and UHP treatments (10.83 , 47.8 , and 19.8 mg , respectively). Furthermore, Fig. 5(d) and 5(e) show that the leaves of lettuce in the UHP and MB/UHP treatments were stronger and greener than those in the CK and MB treatments. These results suggest that MB/UHP not only could degrade SMX in soil but also promote crop growth, which overcomes the current limitation of repair technologies that only focus on soil repair and ignore crop production.

3.5. QSAR model results and interpretation

The preceding results showed that MB/UHP had a positive degradation effect on SMX. To further verify the catalytic degradation efficiency of MB/UHP, we tested 19 antibiotics with different structures, including Adamantan-1-amine, Sulfapyridine, Sulfadiazine, Sulfamethoxazole, Sulfathiazole, Sulfamerazine, Sulfisoxazole, Sulfamethizole, Sulfamethazine, Sulfamonomethoxine, Sulfameter, Sulfamethoxypyridazine, Sulfachloropyridazine, Sulfadimoxine, Norfloxacin, Sulfadimethoxypyrimidine, Ciprofloxacin, Enrofloxacin, and Ofloxacin. Detailed structures of 19 antibiotics and their quantum chemical parameters are shown in Fig. S12 and Table S5. Fig. 6 presents the removal rate (Re%) of 19 antibiotics by MB/UHP. The Re% values of these

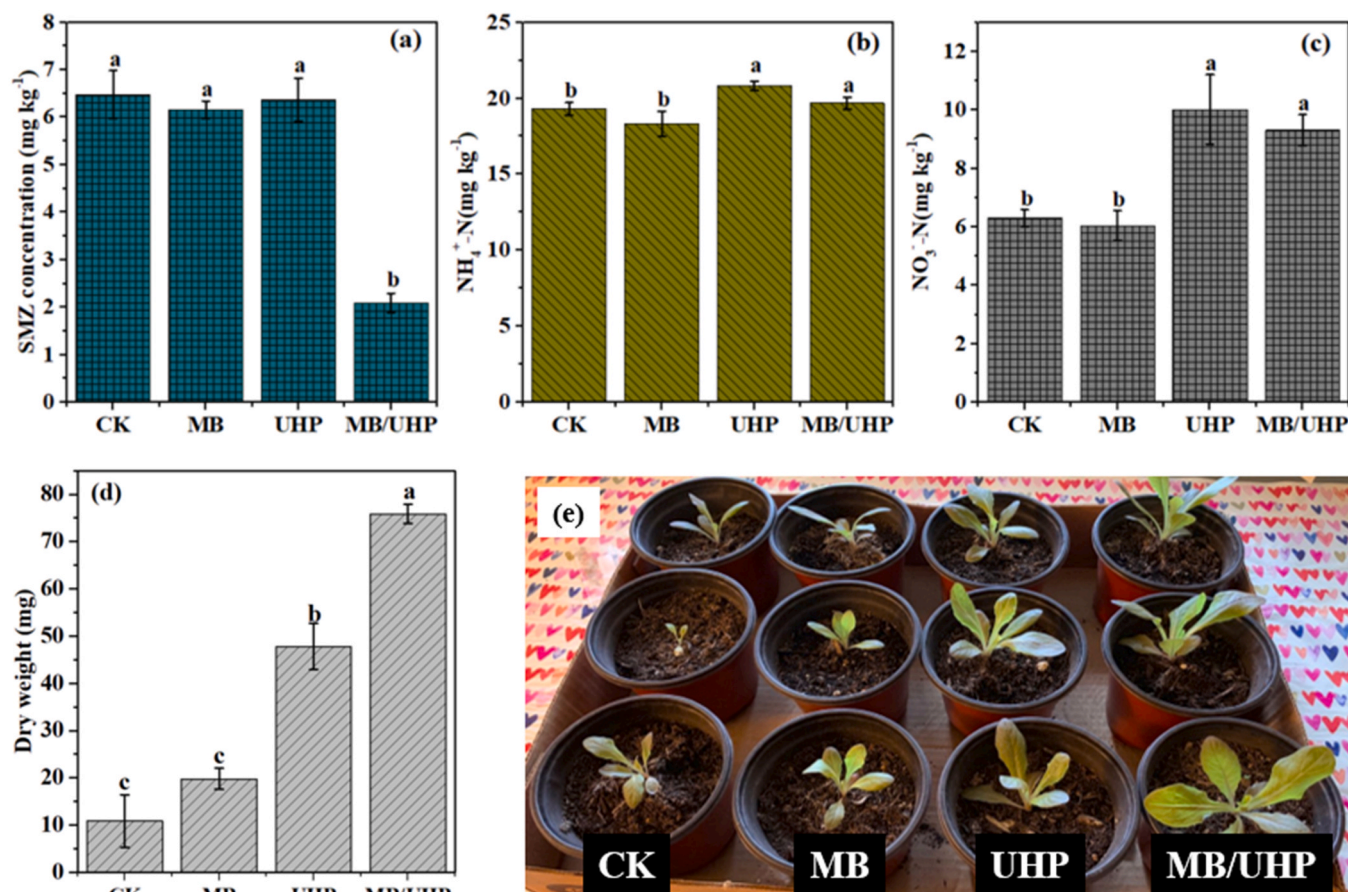


Fig. 5. The effect of MB, UHP and MB/UHP on the concentration of SMZ (a), NH₄⁺-N (b), NO₃⁻-N (c) in soil, dry weight of plant (d) and lettuce growth (e).

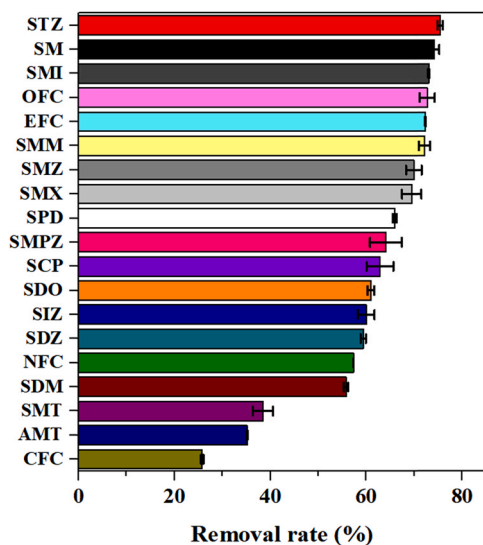


Fig. 6. Removal rate (%) of 19 kinds of antibiotics by MB1/UHP.

Table 1

Regression models for calculating Re% of 19 antibiotics.

No.	Model	R ²	SD	q ²	F	sig.	RMSE	Q _{ext} ²
1	Re% = 1.016 - 0.043 μ	0.768	0.069	0.648	49.728	0.000	0.005	0.728
2	Re% = 1.895 - 0.050 μ + 3.418 E _{HOMO}	0.818	0.064	0.696	24.638	0.000	0.004	0.733
3	Re% = -0.228 to 0.046 μ + 3.643 E _{HOMO} + 1.113 BO _x	0.877	0.055	0.760	23.711	0.000	0.003	0.897

antibiotics demonstrate a significant difference, ranging from 25.8% of ciprofloxacin to 75.4% of sulfathiazole. This result may be due to the various molecular structures of antibiotics. To verify the effect of the structural factors on the Re% of antibiotics, we developed the QSAR models.

Table 1 shows the results of three QSAR models for Re% and associated statistical indices. For all the three models, $R^2 > 0.6$, $q^2 > 0.5$, and $Q_{ext}^2 > 0.5$, which means that they conform to the statistical criteria [50, 51]. To better predict the Re% of antibiotics during the catalytic degradation by MB/UHP, we selected model 3 as the optimal QSAR model because it had the largest R^2 , q^2 , and Q_{ext}^2 values, and the smallest SD and RMSE values. The sig. value also suggests that the variables in model 3 differ and that this model has a significant statistical significance (Table 1). The high F values (i.e., 23.711) indicate that the null hypothesis can be eliminated.

Additionally, t and VIF tests were performed to verify if the variables in model 3 were within reason. As shown in Table S6, all the absolute t values are larger than the reference value (i.e., 1.771, $p \leq 0.01$). The VIF value of each variable confirms that no multicollinearity exists between the three variables in model 3. All the R^2 and q^2 values in the new models are much smaller than those in model 3 (Fig. S13), which means that the optimal QSAR model is robust and there is no possibility of

chance correlation. A plot of experimental and predicted Re% values is shown in Fig. 7(a). The average difference of compounds in the training set is $-0.009 \pm 0.048\%$. The training set compounds (i.e., black square points) show an excellent agreement between experimental and predicted Re% values. For the test set compounds, Adamantan-1-amine, Enrofloxacin, and Ofloxacin are outside the variation range of the residuals within 10%, while the predicted Re% values of Sulfamerazine and Norfloxacin are consistent with the experimental Re% values. The largest, smallest, and average differences in the test set are 32.338%, 5.857%, and $16.024 \pm 10.589\%$, respectively. The reason is probably that the structure of Adamantan-1-amine is different from that of the other 18 antibiotics (i.e., no sulfonic group exists in Adamantan-1-amine, Fig. S12). To help users assess whether the prediction for a new compound is reliable, we further defined the applicability domain (i.e., APD) (Text S2). Williams plot was used to visualize the APD area for the optimal QSAR model (Fig. 7(b)). Generally, the APD of a QSAR model should be the area with $-3 \leq \sigma \leq 3$ and $h_i < h^*$ [52]. Fig. 7(b) shows only three antibiotics (i.e., Damantan-1-amine, Enrofloxacin, and Ofloxacin) locate outside the APD area (i.e., orange area). However, the leverage values of these compounds are smaller than 0.923 (i.e., warning leverage (h^*)), and the predictions for Enrofloxacin and Ofloxacin fit well with the experimental Re% values, further indicating that model 3 has good generalizability [53]. Taken together, the developed model can be considered reliable, stable, and with good prediction ability.

The optimal QSAR model shows that Re% can be explained by three quantum chemical parameters: μ , E_{HOMO} , and BO_x . First, μ (i.e., dipole moment) manifests the magnitude of the molecular polarity and has a negative relationship with Re%. For example, larger μ values lead to lower Re% except for Damantan-1-amine, whose dipole moment and Re% values are the smallest among the 19 antibiotics (Table S5). A possible reason is that the symmetrical structure of Damantan-1-amine results in high chemical stability.

Second, E_{HOMO} presents the energy of the highest occupied molecular orbital, and is positively correlated with Re%. E_{HOMO} is always associated with the ability to donate electrons; the larger the E_{HOMO} value is, the stronger is the ability of a molecule to donate electrons, thereby leading to faster degradation of the molecule. Recently, E_{HOMO} has been demonstrated as a critical quantum parameter to interpret the chemical/biological behaviors (e.g., reaction rate [54], removal rate [55], and

biological toxicity ($\log EC_{50}$) [56]). Previous studies have also shown that HOMO is correlated to the electron affinity and can be applied as an index to determine the active site of a molecule reacting with other reactants [57].

The last parameter, BO_x , has a positive relationship with Re%, and indicates the stability of the chemical bond between coterminous atoms. In general, larger BO_x values make the chemical bond more stable [55]. Therefore, considering these results, we concluded that μ , E_{HOMO} , and BO_x were the main intrinsic factors influencing Re%.

To better elucidate the degradation mechanism of antibiotics by MBs/UHP, we took SMX as an example and illustrated the degradation process by analyzing HOMO distribution in the parent and each possible intermediate. Fig. 8 presents that the HOMO distribution for SMX mainly spreads over the $-C=C-$ bond in the benzene, leading to the formation of product A by hydroxylation in those two carbon atoms. After calculating the HOMO distribution of product A, the oxidant attacks the area covered by HOMO (i.e., $-C=C-$ bond in the isoxazole) and generates product B. The preceding steps are consistent with the observations from previous experimental results [38]. Interestingly, another $-C=C-$ bond in the hexatomic ring becomes the reactive site and forms product C. The HOMO distribution mainly locates at the $-C=C-$ bond and associated moieties (e.g., $-H$, $-NH_2$, and $-CH_3$) in the first three steps. The MBs/UHP system is mainly involved in the $-OH$ oxidation, which randomly attacks the bonds between carbon and hydrogen atoms (or other unsaturated bonds) [58]. By analyzing the HOMO distribution of product C, the hexatomic ring will be opened and yield product D. Subsequently, product D will take the decarboxylation and generate product E. Then the NH_2CO- headgroup will be attacked, resulting in the formation of product F based on the calculation of product E and the continuous oxidation by $-OH$. The decarboxylation becomes the dominant reaction in the following four steps (see the scheme from product F to I in Fig. 8), leading to the formation of product J, which is confirmed to be a possible product in the degradation of SMX [59]. From the calculation result of product J, the penta-heterocycles are opened and generate product K. Then, cleavage between the CH_3CO- and the other moieties occur based on the distribution of HOMO in product K, followed by the decarboxylation in product L. Finally, product M is further oxidized into small molecules. Although some products in Fig. 8 were not determined in previous experimental studies,

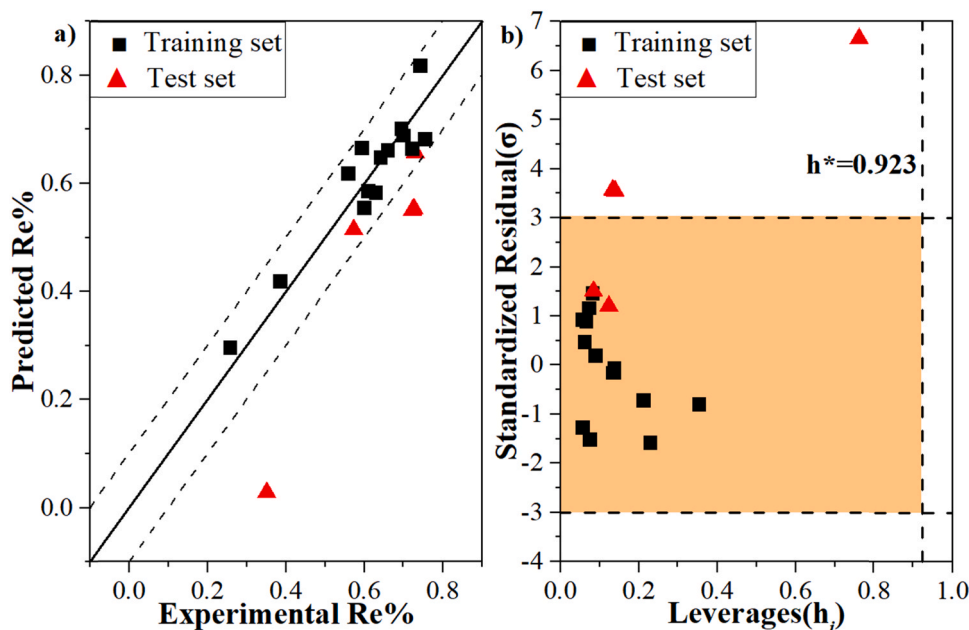


Fig. 7. (a) Comparison of the experimental and predicted Re% values for the training and test sets. The solid line is 1:1, and the dashed lines show the variation range of the residuals within 10%; (b) Williams plot with warning leverages for Model 3.

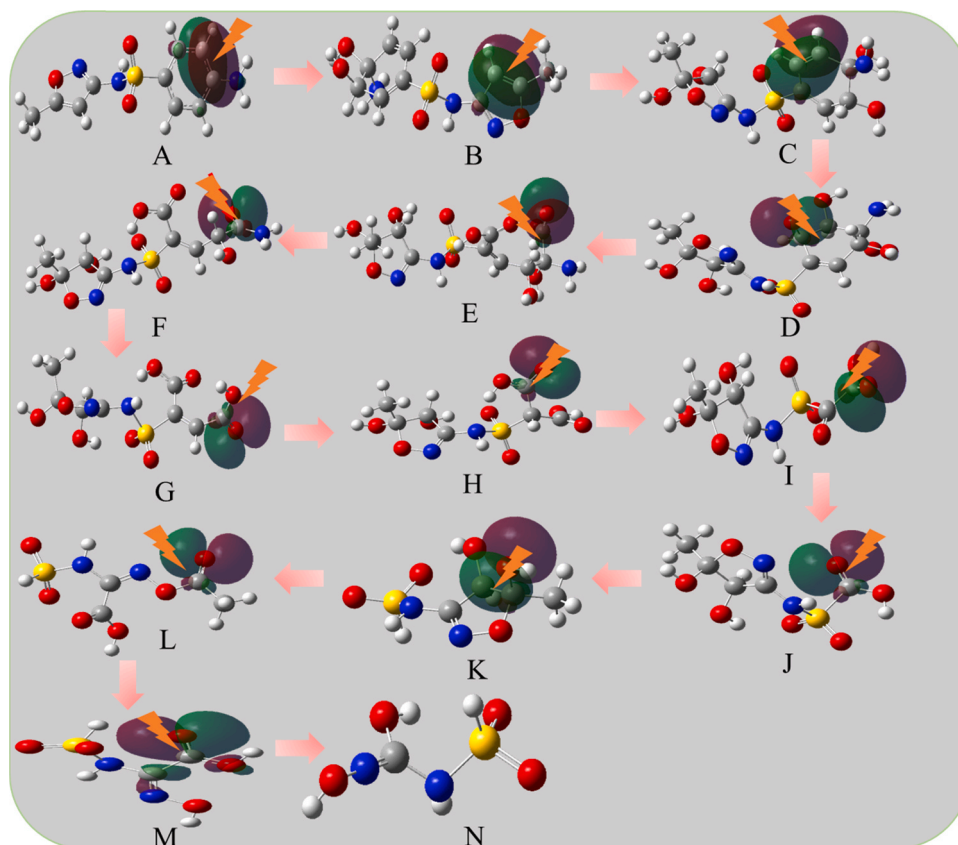


Fig. 8. Proposed degradation pathways of SMX by MBs/UHP based on analyzing HOMO distribution.

the proposed degradation pathway based on HOMO distribution provided new insights into the evaluation of the SMX degradation mechanism.

4. Conclusions

In conclusion, MBs were successfully synthesized using the co-precipitation method and exhibited excellent UHP catalytic ability for antibiotic degradation. Adding different weights of biochar does have a positive effect on the magnitude and composition of the crystals on the surface of MBs. The introduction of biochar enhanced the MBs' sorption and catalytic degradation ability compared with pure MgFe-LDH crystals and UHP alone. MB1/UHP with the optimal biochar weight exhibits the highest catalytic degradation ability of 91% for SMX. The reactive species trapping and EPR tests indicated that in addition to radical pathways of $\bullet\text{OH}$ oxidation, the high contribution of SMX degradation came from the non-radical pathway of $^1\text{O}_2$ in the MB/UHP system. Additionally, we also examined the degradation of other 18 antibiotics. The results showed that the MB/UHP system was effective in their degradation (average removal rate was $61.30\% \pm 14.07\%$). Subsequently, QSAR models were developed by using the removal rate of 19 antibiotics as dependent variables and quantum chemical parameters as independent variables. The results of the optimal QSAR model ($\text{Re}\% = -0.228 - 0.046\mu + 3.643 E_{\text{HOMO}} + 1.113 \text{BO}_x$, $R^2 = 0.877$, $q^2 = 0.760$, and $Q_{\text{ext}}^2 = 0.897$) indicated that μ , E_{HOMO} , and BO_x were the intrinsic factors that affect the removal rate. The degradation pathway of SMX in the MB/UHP process was proposed based on the HOMO distribution in both the parent and each intermediate product. The developed QSAR model not only provides a rapid and accurate method to evaluate the removal rate, but also reveals the degradation mechanism and rules for the degradation of antibiotics in the MB/UHP process. In SMX contaminated soil, MB1/UHP significantly decreased the SMX

contaminant content from 6.47 mg kg^{-1} to 2.10 mg kg^{-1} . Simultaneously, the MB1/UHP increased the available nitrogen content in soil and served as a source of nitrogen for plant uptake, thereby stimulating crop growth. One limitation of this study is that MB/UHP was only revalidated in a soil-lettuce system. Further studies with a larger sample size are needed to confirm the reproducibility of our results in various soil-crop systems. In practice application as soil amendment, the characteristic of MgFe-LDH engineered biochar resembled those of the lab-prepared biochar rather than the commercially available one. Future work must evaluate the property stability of engineered biochar produced from large scale commercial production. The effect of this technology on the absorption and transport of antibiotics in plants also requires further research. In general, the concept and findings presented in this study can be used as references for developing new sustainable and eco-friendly strategies to remediate contaminated agricultural soils.

CRediT authorship contribution statement

Qincheng Chen: Conceptualization, Methodology, Data curation, Writing – original draft. **Zhiwen Cheng:** Investigation, Resources, Formal analysis. **Xiaoying Li:** Investigation, Formal analysis. **Chen Wang:** Investigation, Formal analysis. **Lili Yan:** Investigation, Formal analysis. **Guoqing Shen:** Conceptualization, Resources, Supervision, Writing – review & editing, Funding acquisition. **Zhemín Shen:** Resources, Supervision.

Declaration of Competing Interest

The authors declare that they have no known competing financial interests or personal relationships that could have appeared to influence the work reported in this paper.

Acknowledgements

This work was supported by China Postdoctoral Science Foundation (2020M681284) and the National Natural Science Foundation of China (Grant No. 21876109).

Appendix A. Supporting information

Supplementary data associated with this article can be found in the online version at [doi:10.1016/j.apcatb.2021.120866](https://doi.org/10.1016/j.apcatb.2021.120866).

References

- [1] R. Daghrir, P. Drogui, Tetracycline antibiotics in the environment: a review, *Environ. Chem. Lett.* 11 (2013) 209–227, <https://doi.org/10.1007/s10311-013-0404-8>.
- [2] J.G. Bartlett, D.N. Gilbert, B. Spellberg, Seven ways to preserve the miracle of antibiotics, *Clin. Infect. Dis.* 56 (2013) 1445–1450, <https://doi.org/10.1093/cid/cit070>.
- [3] P. Chaturvedi, P. Shukla, B.S. Giri, P. Chowdhary, R. Chandra, P. Gupta, A. Pandey, Prevalence and hazardous impact of pharmaceutical and personal care products and antibiotics in environment: a review on emerging contaminants, *Environ. Res.* 194 (2021), 110664, <https://doi.org/10.1016/j.envres.2020.110664>.
- [4] F. Deng, S. Li, M. Zhou, Y. Zhu, S. Qiu, K. Li, F. Ma, J. Jiang, A biochar modified nickel-foam cathode with iron-foam catalyst in electro-Fenton for sulfamerazine degradation, *Appl. Catal. B Environ.* 256 (2019), 117796, <https://doi.org/10.1016/j.apcatb.2019.117796>.
- [5] C. Zhou, C. Lai, D. Huang, G. Zeng, C. Zhang, M. Cheng, L. Hu, J. Wan, W. Xiong, M. Wen, L. Qin, Highly porous carbon nitride by supramolecular preassembly of monomers for photocatalytic removal of sulfamethazine under visible light driven, *Appl. Catal. B Environ.* 220 (2018) 202–210, <https://doi.org/10.1016/j.apcatb.2017.08.055>.
- [6] Y. Yang, C. Zhang, D. Huang, G. Zeng, J. Huang, C. Lai, C. Zhou, W. Wang, H. Guo, W. Xue, R. Deng, M. Cheng, W. Xiong, Boron nitride quantum dots decorated ultrathin porous g-C₃N₄: intensified exciton dissociation and charge transfer for promoting visible-light-driven molecular oxygen activation, *Appl. Catal. B Environ.* 245 (2019) 87–99, <https://doi.org/10.1016/j.apcatb.2018.12.049>.
- [7] P.T. Almazán-Sánchez, S. Cotillas, C. Sáez, M.J. Solache-Ríos, V. Martínez-Miranda, P. Cañizares, I. Linares-Hernández, M.A. Rodrigo, Removal of pendimethalin from soil washing effluents using electrolytic and electro-irradiated technologies based on diamond anodes, *Appl. Catal. B Environ.* 213 (2017) 190–197, <https://doi.org/10.1016/j.apcatb.2017.05.008>.
- [8] P. Song, G. Huang, C. An, X. Xin, P. Zhang, X. Chen, X. Yang, Exploring the decentralized treatment of sulfamethoxazole-contained poultry wastewater through vertical-flow multi-soil-layering systems in rural communities, *Water Res.* 188 (2021), 116480, <https://doi.org/10.1016/j.watres.2020.116480>.
- [9] Z. Zhou, J. Ma, X. Liu, C. Lin, K. Sun, H. Zhang, G. Fan, Activation of peroxydisulfate by nanoscale zero-valent iron for sulfamethoxazole removal in agricultural soil: effect, mechanism and ecotoxicity, *Chemosphere* 223 (2019) 196–203, <https://doi.org/10.1016/j.chemosphere.2019.02.074>.
- [10] Y. Yao, B. Gao, J. Fang, M. Zhang, H. Chen, Y. Zhou, A.E. Creamer, Y. Sun, L. Yang, Characterization and environmental applications of clay-biochar composites, *Chem. Eng. J.* 242 (2014) 136–143, <https://doi.org/10.1016/j.cej.2013.12.062>.
- [11] J. Qin, Y. Cheng, M. Sun, L. Yan, G. Shen, Catalytic degradation of the soil fumigant 1,3-dichloropropene in aqueous biochar slurry, *Sci. Total Environ.* 569–570 (2016) 1–8, <https://doi.org/10.1016/j.scitotenv.2016.06.092>.
- [12] C. Zhao, B. Shao, M. Yan, Z. Liu, Q. Liang, Q. He, T. Wu, Y. Liu, Y. Pan, J. Huang, J. Wang, J. Liang, L. Tang, Activation of peroxymonosulfate by biochar-based catalysts and applications in the degradation of organic contaminants: a review, *Chem. Eng. J.* 416 (2021), 128829, <https://doi.org/10.1016/j.cej.2021.128829>.
- [13] G. Fang, C. Liu, J. Gao, D.D. Dionysiou, D. Zhou, Manipulation of persistent free radicals in biochar to activate persulfate for contaminant degradation, *Environ. Sci. Technol.* 49 (2015) 5645–5653, <https://doi.org/10.1021/es5061512>.
- [14] R.S. Varma, K.P. Naicker, The urea–hydrogen peroxide complex: solid-state oxidative protocols for hydroxylated aldehydes and ketones (Dakin reaction), nitriles, sulfides, and nitrogen heterocycles, *Org. Lett.* 1 (1999) 189–192, <https://doi.org/10.1021/ol990522n>.
- [15] S.C. Laha, R. Kumar, Selective epoxidation of styrene to styrene oxide over TS-1 using urea–hydrogen peroxide as oxidizing agent, *J. Catal.* 204 (2001) 64–70, <https://doi.org/10.1006/jcat.2001.3352>.
- [16] W.T. Frabknsberger, Factors affecting the urea peroxide added to soil, *Bull. Environ. Contam. Toxicol.* 59 (1997) 50–57.
- [17] J. Qin, D.J. Ashworth, S.R. Yates, G. Shen, Coupled use of Fe-impregnated biochar and urea–hydrogen peroxide to simultaneously reduce soil–air emissions of fumigant and improve crop growth, *J. Hazard. Mater.* 396 (2020), 122762, <https://doi.org/10.1016/j.jhazmat.2020.122762>.
- [18] D. Kang, X. Yu, S. Tong, M. Ge, J. Zuo, C. Cao, W. Song, Performance and mechanism of Mg/Fe layered double hydroxides for fluoride and arsenate removal from aqueous solution, *Chem. Eng. J.* 228 (2013) 731–740, <https://doi.org/10.1016/j.cej.2013.05.041>.
- [19] X. Tan, S. Liu, Y. Liu, Y. Gu, G. Zeng, X. Cai, Z. Yan, C. Yang, X. Hu, B. Chen, One-pot synthesis of carbon supported calcined-Mg/Al layered double hydroxides for antibiotic removal by slow pyrolysis of biomass waste, *Sci. Rep.* 6 (2016) 1–6, <https://doi.org/10.1038/srep39691>.
- [20] R. Guo, Y. Li, Y. Chen, Y. Liu, B. Niu, J. Gou, X. Cheng, Efficient degradation of sulfamethoxazole by CoCu LDH composite membrane activating peroxymonosulfate with decreased metal ion leaching, *Chem. Eng. J.* 417 (2021), 127887, <https://doi.org/10.1016/j.cej.2020.127887>.
- [21] S. Luo, Z. Wei, D.D. Dionysiou, R. Spinney, W.P. Hu, L. Chai, Z. Yang, T. Ye, R. Xiao, Mechanistic insight into reactivity of sulfate radical with aromatic contaminants through single-electron transfer pathway, *Chem. Eng. J.* 327 (2021) 1056–1065, <https://doi.org/10.1016/j.cej.2017.06.179>.
- [22] Z. Cheng, B. Yang, Q. Chen, X. Gao, Y. Tan, Y. Ma, Z. Shen, A quantitative-structure-activity-relationship (QSAR) model for the reaction rate constants of organic compounds during the ozonation process at different temperatures, *Chem. Eng. J.* 353 (2018) 288–296, <https://doi.org/10.1016/j.cej.2018.07.122>.
- [23] Z. Cheng, Q. Chen, S. Cervantes, Q. Tang, X. Gao, Y. Tan, S. Liu, Y. Ma, Z. Shen, Two-dimensional and three-dimensional quantitative structure-activity relationship models for the degradation of organophosphate flame retardants during supercritical water oxidation, *J. Hazard. Mater.* 394 (2020), 121811, <https://doi.org/10.1016/j.jhazmat.2019.121811>.
- [24] P. Su, H. Zhu, Z. Shen, QSAR models for removal rates of organic pollutants adsorbed by in situ formed manganese dioxide under acid condition, *Environ. Sci. Pollut. Res.* 23 (2016) 3609–3620.
- [25] Z. Cheng, Q. Chen, F.W. Pontius, X. Gao, Y. Tan, Y. Ma, Z. Shen, Two new predictors combined with quantum chemical parameters for the selection of oxidants and degradation of organic contaminants: a QSAR modeling study, *Chemosphere* 240 (2020), 124928, <https://doi.org/10.1016/j.chemosphere.2019.124928>.
- [26] Y. Huang, T. Li, S. Zheng, L. Fan, L. Su, Y. Zhao, H. Xie, C. Li, QSAR modeling for the ozonation of diverse organic compounds in water, *Sci. Total Environ.* 715 (2020), 136816, <https://doi.org/10.1016/j.scitotenv.2020.136816>.
- [27] T. Ye, Z. Wei, R. Spinney, C.J. Tang, S. Luo, R. Xiao, D.D. Dionysiou, Chemical structure-based predictive model for the oxidation of trace organic contaminants by sulfate radical, *Water Res.* 116 (2017) 106–115, <https://doi.org/10.1016/j.watres.2017.03.015>.
- [28] C. Li, H.B. Xie, J. Chen, X. Yang, Y. Zhang, X. Qiao, Predicting gaseous reaction rates of short chain chlorinated paraffins with •OH: overcoming the difficulty in experimental determination, *Environ. Sci. Technol.* 48 (2014) 13808–13816, <https://doi.org/10.1021/es504339r>.
- [29] X. Huang, Y. Feng, C. Hu, X. Xiao, D. Yu, X. Zou, Mechanistic QSAR models for interpreting degradation rates of sulfonamides in UV-photocatalysis systems, *Chemosphere* 138 (2015) 183–189, <https://doi.org/10.1016/j.chemosphere.2015.05.075>.
- [30] X. Luo, X. Wei, J. Chen, Q. Xie, X. Yang, W.J. Peijnenburg, Rate constants of hydroxyl radicals reaction with different dissociation species of fluoroquinolones and sulfonamides: combined experimental and QSAR studies, *Water Res.* 166 (2019), 115083, <https://doi.org/10.1016/j.watres.2019.115083>.
- [31] M.J. Frisch, G.W. Trucks, H.B. Schlegel, G.E. Scuseria, M.A. Robb, J.R. Cheeseman, G. Scalmani, V. Barone, B. Mennucci, G.A. Petersson, H. Nakatsuji, M. Caricato, X. Li, H.P. Hratchian, A.F. Izmaylov, J. Bloino, G. Zheng, J.L. Sonnenberg, M. Hada, E. M. K. Toyota, R. Fukuda, J. Hasegawa, M. Ishida, T. Nakajima, Y. Honda, K. O., H. Nakai, T. Vreven, J.A.J. Montgomery, J.E. Peralta, F. Ogliaro, M. Bearpark, J.J. Heyd, E. Brothers, K.N. Kudin, V.N. Staroverov, R. Kobayashi, J. Normand, K. Raghavachari, A. Rendell, J.C. Burant, S.S. Iyengar, J. Tomasi, M. Cossi, N. Rega, M.J. Millam, M. Klene, J.E. Knox, J.B. Cross, V. Bakken, C. Adamo, J. Jaramillo, R. Gomperts, R.E. Stratmann, O. Yazyev, A.J. Austin, R. Cammi, C. Pomelli, J.W. Ochterski, R.L. Martin, K. Morokuma, V.G. Zakrzewski, F. Salvador, J.J. Dannenberg, S. Dapprich, A.D. Daniels, O. Farkas, J.B. Foresman, J.V. Ortiz, J. Cioslowski, D.J. Fox, Gaussian 09 Revision A.02, Gaussian Inc. Wallingford, CT. (2009).
- [32] B. Delley, From molecules to solids with the DMol3 approach, *J. Chem. Phys.* 113 (2000) 7756–7764, <https://doi.org/10.1063/1.1316015>.
- [33] Q. Tao, Y. Zhang, X. Zhang, P. Yuan, H. He, Synthesis and characterization of layered double hydroxides with a high aspect ratio, *J. Solid State Chem.* 179 (2006) 708–715, <https://doi.org/10.1016/j.jssc.2005.11.023>.
- [34] L. Xue, B. Gao, Y. Wan, J. Fang, S. Wang, Y. Li, R. Muñoz-Carpena, L. Yang, High efficiency and selectivity of MgFe-LDH modified wheat-straw biochar in the removal of nitrate from aqueous solutions, *J. Taiwan Inst. Chem. Eng.* 63 (2016) 312–317, <https://doi.org/10.1016/j.jtice.2016.03.021>.
- [35] D. Ding, S. Yang, X. Qian, L. Chen, T. Cai, Nitrogen-doping positively whilst sulfur-doping negatively affect the catalytic activity of biochar for the degradation of organic contaminant, *Appl. Catal. B Environ.* 263 (2020), <https://doi.org/10.1016/j.apcatb.2019.118348>.
- [36] G. Fang, C. Liu, Y. Wang, D.D. Dionysiou, D. Zhou, Photogeneration of reactive oxygen species from biochar suspension for diethyl phthalate degradation, *Appl. Catal. B Environ.* 214 (2017) 34–45, <https://doi.org/10.1016/j.apcatb.2021.120417>.
- [37] Y. Bao, T.-T. Lim, R. Wang, R.D. Webster, X. Hu, Urea-assisted one-step synthesis of cobalt ferrite impregnated ceramic membrane for sulfamethoxazole degradation via peroxymonosulfate activation, *Chem. Eng. J.* 343 (2018) 737–747, <https://doi.org/10.1016/j.cej.2018.03.010>.
- [38] Y. Bao, W.D. Oh, T.T. Lim, R. Wang, R.D. Webster, X. Hu, Elucidation of stoichiometric efficiency, radical generation and transformation pathway during catalytic oxidation of sulfamethoxazole via peroxymonosulfate activation, *Water Res.* 151 (2019) 64–74, <https://doi.org/10.1016/j.watres.2018.12.007>.

- [39] Y. Liu, Q. Fan, J. Wang, Zn-Fe-CNTs catalytic in situ generation of H₂O₂ for Fenton-like degradation of sulfamethoxazole, *J. Hazard. Mater.* 342 (2018) 166–176, <https://doi.org/10.1016/j.jhazmat.2017.08.016>.
- [40] T. Charbouillot, M. Brigante, G. Mailhot, P.R. Maddigapu, C. Minero, D. Vione, Performance and selectivity of the terephthalic acid probe for OH as function of temperature, pH and composition of atmospherically relevant aqueous media, *J. Photochem. Photobiol. A* 222 (2011) 70–76, <https://doi.org/10.1016/j.jphotochem.2011.05.003>.
- [41] S. Ye, G. Zeng, X. Tan, H. Wu, J. Liang, B. Song, Ning Tang, Peng Zhang, Yuanyuan Yang, Qiang Chen, X. Li, Nitrogen-doped biochar fiber with graphitization from *Boehmeria nivea* for promoted peroxymonosulfate activation and non-radical degradation pathways with enhancing electron transfer, *Appl. Catal. B Environ.* 269 (2020), 118850, <https://doi.org/10.1016/j.apcatb.2020.118850>.
- [42] G. Peng, W. You, W. Zhou, G. Zhou, C. Qi, Y. Hua, Activation of peroxymonosulfate by phosphite: kinetics and mechanism for the removal of organic pollutants, *Chemosphere* 266 (2021), 129016, <https://doi.org/10.1016/j.chemosphere.2020.129016>.
- [43] A. Ivanets, M. Roshchina, V. Srivastava, V. Prozorovich, T. Dontsova, S. Nahirniak, V. Pankov, A. Hosseini-Bandegharai, H. Tran, M. Sillanpää, Effect of metal ions adsorption on the efficiency of methylene blue degradation onto MgFe₂O₄ as Fenton-like catalysts, *Colloids Surf. A Physicochem. Eng. Asp.* 571 (2019) 17–26, <https://doi.org/10.1016/j.colsurfa.2019.03.071>.
- [44] S. Agrawal, N. Nirwan, A. Chohadia, Degradation of acriflavine using environmentally benign process involving singlet-oxygen-photo-Fenton: a comparative study, *J. Photochem. Photobiol. A* 398 (2020), 112547, <https://doi.org/10.1016/j.jphotochem.2020.112547>.
- [45] T. Li, L. Ge, X. Peng, W. Wang, W. Zhang, Enhanced degradation of sulfamethoxazole by a novel Fenton-like system with significantly reduced consumption of H₂O₂ activated by g-C₃N₄/MgO composite, *Water Res.* 190 (2021), 116777, <https://doi.org/10.1016/j.watres.2020.116777>.
- [46] X.Y. Tang, W.D. Huang, J.J. Guo, Y. Yang, R. Tao, X. Feng, Use of Fe-impregnated biochar to efficiently sorb chlorpyrifos, reduce uptake by *Allium fistulosum* L., and enhance microbial community diversity, *J. Agric. Food Chem.* 65 (2017) 5238–5243.
- [47] J.H. Bryce, D.D. Focht, L.H. Stolzy, Soil aeration and plant growth response to urea peroxide fertilization, *Soil Sci.* 134 (1982) 111–116.
- [48] B.P. Singh, B.J. Hatton, B. Singh, A.L. Cowie, A. Kathuria, Influence of biochars on nitrous oxide emission and nitrogen leaching from two contrasting soils, *J. Environ. Qual.* 39 (2010) 1224–1235, <https://doi.org/10.2134/jeq2009.0138>.
- [49] Y. Yao, B. Gao, J. Chen, L. Yang, Engineered biochar reclaiming phosphate from aqueous solutions: mechanisms and potential application as a slow-release fertilizer, *Environ. Sci. Technol.* 47 (2013) 8700–8708, <https://doi.org/10.1021/es4012977>.
- [50] A. Tropsha, P. Gramatica, V.K. Gombar, The importance of being earnest: Validation is the absolute essential for successful application and interpretation of QSPR models, *QSAR Comb. Sci.* 22 (2003) 69–77, <https://doi.org/10.1002/qsar.200390007>.
- [51] R. Xiao, T. Ye, Z. Wei, S. Luo, Z. Yang, R. Spinney, Quantitative structureactivity relationship (QSAR) for the oxidation of trace organic contaminants by sulfate radical, *Environ. Sci. Technol.* 49 (2015) 13394–13402, <https://doi.org/10.1021/acs.est.5b03078>.
- [52] J. Jaworska, N. Nikolova-Jeliazkova, T. Aldenberg, QSAR applicability domain estimation by projection of the training set in descriptor space: a review, *Altern. Lab. Anim.* 33 (2005) 445–459, <https://doi.org/10.1177/026119290503300508>.
- [53] Y. Wang, J. Chen, X. Li, B. Wang, X. Cai, L. Huang, Predicting rate constants of hydroxyl radical reactions with organic pollutants: algorithm, validation, applicability domain, and mechanistic interpretation, *Atmos. Environ.* 43 (2009) 1131–1135, <https://doi.org/10.1016/j.atmosenv.2008.11.012>.
- [54] H. Zhu, Z. Shen, Q. Tang, W. Ji, L. Jia, Degradation mechanism study of organic pollutants in ozonation process by QSAR analysis, *Chem. Eng. J.* 255 (2014) 431–436, <https://doi.org/10.1016/j.cej.2014.05.073>.
- [55] P. Su, H. Zhu, Z. Shen, QSAR models for removal rates of organic pollutants adsorbed by in situ formed manganese dioxide under acid condition, *Environ. Sci. Pollut. Res.* 23 (2016) 3609–3620, <https://doi.org/10.1007/s11356-015-5569-1>.
- [56] W. Gu, Y. Zhao, Q. Li, Y. Li, Environmentally friendly polychlorinated naphthalenes (PCNs) derivatives designed using 3D-QSAR and screened using molecular docking, density functional theory and health-based risk assessment, *J. Hazard. Mater.* 363 (2019) 316–327, <https://doi.org/10.1016/j.jhazmat.2018.09.060>.
- [57] X. Xu, J. Chen, S. Wang, J. Ge, R. Qu, M. Feng, V.K. Sharma, Z. Wang, Degradation kinetics and transformation products of chlorophene by aqueous permanganate, *Water Res.* 138 (2018) 293–300, <https://doi.org/10.1016/j.watres.2018.03.057>.
- [58] Y.T. Chen, W.R. Chen, T.F. Lin, Oxidation of cyanobacterial neurotoxin beta-N-methylamino-L-alanine (BMAA) with chlorine, permanganate, ozone, hydrogen peroxide and hydroxyl radical, *Water Res.* 142 (2018) 187–194, <https://doi.org/10.1016/j.watres.2018.05.056>.
- [59] R. Yin, W. Guo, H. Wang, J. Du, Q. Wu, J.S. Chang, N. Ren, Singlet oxygen-dominated peroxydisulfate activation by sludge-derived biochar for sulfamethoxazole degradation through a nonradical oxidation pathway: performance and mechanism, *Chem. Eng. J.* 357 (2019) 589–599, <https://doi.org/10.1016/j.cej.2018.09.184>.